Rheol Acta (2005) 44: 219–234
DOI 10.1007/s00397-004-0377-4

ORIGINAL CONTRIBUTION

Xiaoyu Zheng
M. Gregory Forest
Ruhai Zhou
Qi Wang

Likelihood and expected-time statistics of monodomain attractors in sheared discotic and rod-like nematic polymers

Received: 17 December 2003
Accepted: 6 April 2004
Published online: 9 June 2004

X. Zheng · M. G. Forest (✉) · R. Zhou
Department of Mathematics,
University of North Carolina at Chapel Hill, Chapel Hill, NC 27599–3250, USA
E-mail: forest@amath.unc.edu
Tel.: +1-919-9629606
Fax: +1-919-9629345

Q. Wang
Department of Mathematics,
Florida State University,
Tallahassee, FL 32306–4510, USA

Abstract Employing a mesoscopic Doi tensor model, we develop transient statistical properties of sheared nematic polymer monodomains consistent with typical experimental protocols. Our goal is to convey to the experimentalist a list of expected outcomes, based not only on properties of the nematic liquid and imposed flow rate, but also on the timescale of the experiment and variability in the initial conditions. Step 1 is deterministic: we solve the model equations completely, then compile the flow-phase diagram of all monodomain attractors and phase transitions versus nematic concentration and Peclet number (shear rate normalized by molecular relaxation rate). Step 2 is to overlay on the phase diagram a statistical diagnostic of the expected time, $\langle t \rangle_{\mathbf{A}}$, to reach a small neighborhood of every attractor **A**. The statistics are taken over the arbitrary quiescent director angle on the sphere, modeling experiments that begin from rest. Step 3 is to explore parameter regimes with multiple attractors, where we statistically determine the likelihood of convergence to each attractor. These statistical properties are critical for any application of theoretical models to the interpretation of experimental data. If $\langle t \rangle_{\mathbf{A}}$ is longer than the timescale of the experiment, attractor **A** is never fully resonated and the relevant stress and scattering predictions are those of the transients, not the attractor. In bi-stable and tri-stable parameter regimes, which are typical of nematic polymers, a distribution of monodomains of each type will populate the sample, so experimental data must be compared with weighted averages based on the likelihood of each attractor (see Grosso et al (2003) Phys Rev Lett 90:098304). The final step is to give statistics of shear stress and normal stress differences during the approach to each attractor type, as well as typical paths of the major director that are contrasted with the results of Van Horn et al (Rheol Acta (2003) 42(6):585–589) with Leslie-Ericksen theory.

Keywords Nematic polymers · Shear flow · Transient rheology

Introduction

In confined flows of initially homogenous nematic polymers, a key factor in the evolution of mesostructure is the likely timescale, denoted by $\langle t \rangle_{\mathbf{A}}$, on which monodomain mesophase attracting states, denoted by **A**, are resonated by the imposed flow. These monodomain modes (flow-aligning (**FA**), logrolling (**LR**), tumbling

(**T**), wagging (**W**), kayaking (**K**), chaotic (**CH**)) are important precursors to the onset and generation of structure *if* they are given the time to set up in the interior of the flow sample. Flow-induced monodomain attractors are expected in experiments if the following all hold: (1) the experiment is longer than $\langle t \rangle_{\mathbf{A}}$ for the relevant attractor(s) **A**; (2) the initial sample is not riddled with defects; (3) $\langle t \rangle_{\mathbf{A}} < t_\partial$ where t is the timescale on which boundary layers induced by anchoring conditions (at plates, solid boundaries, or even pinned defects) propagate to the interior and alter the pure shear response of local monodomains. When $\langle t \rangle_{\mathbf{A}} > t_\partial$, nonhomogeneities generate a more complex evolution, and the monodomain restriction is not valid due to strong spatial mode coupling. For small molecule nematic polymers in plane Couette cells, this condition ($\langle t \rangle_{\mathbf{A}} < t_\partial$) is typically satisfied and MD modes are well documented on experimental timescales. Several authors [1, 2, 3, 4] have studied the transitions from initial quiescent nematic liquids to monodomain attractors. *The purpose of this study is to provide statistical diagnostics for the expected time,* $\langle t \rangle_{\boldsymbol{A}}$*, required to resonate MD attractor* $\boldsymbol{A}$ *in sheared nematic polymers, for all attractor types* **FA**, **LR**, **T**, **W**, **K**, **CH**. We perform statistical averaging over typical experimental initial conditions: the set of quiescent nematic equilibria when the experiment begins at rest.

We develop these diagnostics using a standard mesoscopic tensor model. In particular, we begin by computing the flow phase diagram of MD attractors, then overlay the expected time, $\langle t \rangle_{\mathbf{A}}$, required to converge to attractors from the orientationally degenerate nematic rest state. We study dynamics of confined in-plane versus full orientation tensors, which allows us to easily flag the slowest decaying tensor modes for in-plane attractors (**FA**, **T**, **W**, **LR**) across the phase diagram, and to flag which in-plane solutions are unstable to out-of-plane perturbations. Finally, for bi-stable and tri-stable parameter regimes, we determine which pre-aligned quiescent equilibria converge to which attractor (their respective domains of attraction), and monitor rheological properties of the transient orbits during their evolution, following [3].

Model description and background results

To lay the groundwork for this paper, we recall and extend results from [5] for the particular mesoscopic tensor model that derives from the Doi kinetic theory with quadratic closure. We begin with the solution space of this model – the flow-phase diagrams of monodomain attractors versus two dimensionless parameters: a concentration parameter N, which controls the strength of the excluded volume potential; and the Peclet number $Pe = \dot{\gamma}/6D_{\mathrm{r}}^0$, where $\dot{\gamma}$ is the imposed shear rate and $6D_{\mathrm{r}}^0$ is the average rotational relaxation rate. The remaining model parameter is a molecule aspect ratio parameter $a = \frac{r^2-1}{r^2+1}$, where r is the aspect ratio. We choose a 3:1 or 1:3 aspect ratio for spheroidal molecules, for which $a = \pm 0.8$, since the resulting dynamical system qualitatively captures representative features of the kinetic phase diagram [6, 7, 8, 9, 10]. Mesoscopic models of [11] and [12] display similar phase diagrams.

The kinetic and mesoscopic equations have a symmetry which implies that monodomain responses of rods and platelets are equivalent up to a pure rotation of the *pdf* or the **Q** tensor [13, 5]. Therefore, results presented here for monodomain responses to pure shear may be applied to rod-like or discotic nematic polymers. Although the second-moment tensors of rod-like and discotic liquids are simply related, their stresses are not, which we illustrate below.

These tensor models are equivalent to a 5-dimensional ordinary differential equation (ODE) for the components

$$\vec{Q} = (Q_{xx}, Q_{xy}, Q_{yy}, Q_{xz}, Q_{yz}) \tag{1}$$

of the symmetric, trace zero, second-moment tensor **Q**. All closures of the Doi kinetic theory for monodomain response to imposed linear flow take the form [5]:

$$\dot{\boldsymbol{Q}} = \boldsymbol{F}(\boldsymbol{Q}; N, a) + PeG(Q; JV; a) \tag{2}$$

where time is normalized by the nematic timescale $\left(6D_{\mathrm{r}}^0\right)^{-1}$, Pe and N are defined earlier, and for pure shear flow in dimensional coordinates,

$$\mathbf{v}_{\mathrm{shear}} = \dot{\gamma}(y, 0, 0), \quad \nabla \mathbf{v} = \Omega + \mathbf{D} = \dot{\gamma} \begin{pmatrix} 0 & 1 & 0 \\ 0 & 0 & 0 \\ 0 & 0 & 0 \end{pmatrix}. \tag{3}$$

The precise form of **F**, **G** for the Doi closure model are [5]:

$$\begin{aligned} \mathbf{F} &= \mathbf{Q} - N\left(\mathbf{Q} + \frac{\mathbf{I}}{3}\right) \cdot \mathbf{Q} + N\mathbf{Q} : \left(\mathbf{Q} + \frac{\mathbf{I}}{3}\right)\left(\mathbf{Q} + \frac{\mathbf{I}}{3}\right), \\ \mathbf{G} &= \Omega \cdot \mathbf{Q} - \mathbf{Q} \cdot \Omega + a(\mathbf{D} \cdot \mathbf{Q} + \mathbf{Q} \cdot \mathbf{D}) \\ &\quad + \left(\frac{3a}{2}\mathbf{D} - \mathbf{D} : \left(\mathbf{Q} + \frac{\mathbf{I}}{3}\right)\left(\mathbf{Q} + \frac{\mathbf{I}}{3}\right)\right). \end{aligned} \tag{4}$$

Physically, **F** captures the mesoscopic approximation of the Maier-Saupe intermolecular potential, while **G** represents the flow-induced orientational response for linear velocity fields.

Q has eigenvalues $d_i - 1/3$, with corresponding eigenvectors $\vec{n}_i, i = 1, 2, 3$, ordered by $0 \le d_3 \le d_2 \le d_1 \le 1$. When d_1 is simple, $\vec{n}_1$ is called the major director. Otherwise, if $d_1 = d_2$, such **Q** tensors are labeled as

defects, corresponding to orientation states for which the peak orientation direction is degenerate. If $d_1 = d_2 \neq d_3$, then the eigenspace of the major director is the unit circle in the plane orthogonal to $\vec{n}_3$. If $d_1 = d_2 = d_3$, then $\mathbf{Q} \equiv 0$ and the phase is isotropic.

In-plane orientation states are distinguished by the property that the major director $\vec{n}_1$ lies in the flow deformation plane (x,y), which we state by the condition $\vec{n}_1 \perp \vec{e}_z$, where $\vec{e}_z$ is the vorticity axis; *logrolling states* have $\vec{n}_1 // \vec{e}_z$, with peak orientation along the vorticity axis.

In-plane and logrolling states fall into a special subspace of orientation tensors in planar shear flow, called **in-plane tensors** by a slight abuse of terminology, for which one direction is fixed parallel to the vorticity axis. Since $\mathbf{Q}$ is symmetric, the remaining orthogonal eigenvectors lie in the flow deformation plane (x,y), which we call the shear plane.

The space of in-plane (i-p) symmetric, traceless tensors, $\mathbf{Q}^{\text{i-p}}$, is 3-dimensional, obeying two constraints,

$$Q_{xz} = Q_{yz} = 0. \tag{5}$$

All mesoscopic tensor models in simple shear preserve $\mathbf{Q}^{\text{i-p}}$ as a 3-dimensional invariant subspace, so the orientation dynamics can be studied distilled from the two out-of-plane degrees of freedom. By extension of the analysis and computations in [5] and [7], from the fixed nematic concentration $N = 6$ to *all* N, we construct the flow-phase diagram of all attractors and phase-transition boundaries of the Doi model (2)–(4). Figure 1 gives the phase diagram for dynamics of the in-plane space $\mathbf{Q}^{\text{i-p}}$, then Fig. 2 gives the phase diagram for the full tensor space. The three bifurcation curves emanating from the $Pe = 0$ axis are explained below. We will employ this in-plane system for several purposes:

- As a model for monolayers in which molecular orientations are confined to the shear plane, see [14, 15, 16, 17].
- As a model for dynamics of defect sets, and their role in the transient approach to attractors. This study will appear elsewhere [18].
- As a simpler dynamical system in which we can develop statistical diagnostics for attractor properties.
- When compared with the full tensor model (Fig. 2), the results of Fig. 2 and the diagnostics developed in this paper provide a means to determine: (i) which monodomain solutions are stable in $\mathbf{Q}^{\text{ip}}$, yet unstable to out-of-plane perturbations, and how strong the out-of-plane instabilities are, and (ii) for in-plane solutions (**FA**, **T** or **W**, **LR**) stable in the full tensor space, whether the slowest modes of decay to the attractor are in-plane or out-of-plane.

Our primary goal here is to determine the "*strength*" and "*likelihood*" of attractors. A secondary goal is to clarify the timescale on which in-plane stable response will build up out-of-plane instabilities and depart from the shearing plane. There are several ways we might quantify "*strength*", where strong versus weak is based on the rapid versus slow rate of approach to an attractor. We first consider the in-plane attractors from Fig. 1, with $Q_{xz} = Q_{yz} = 0$, to develop the statistical tools.

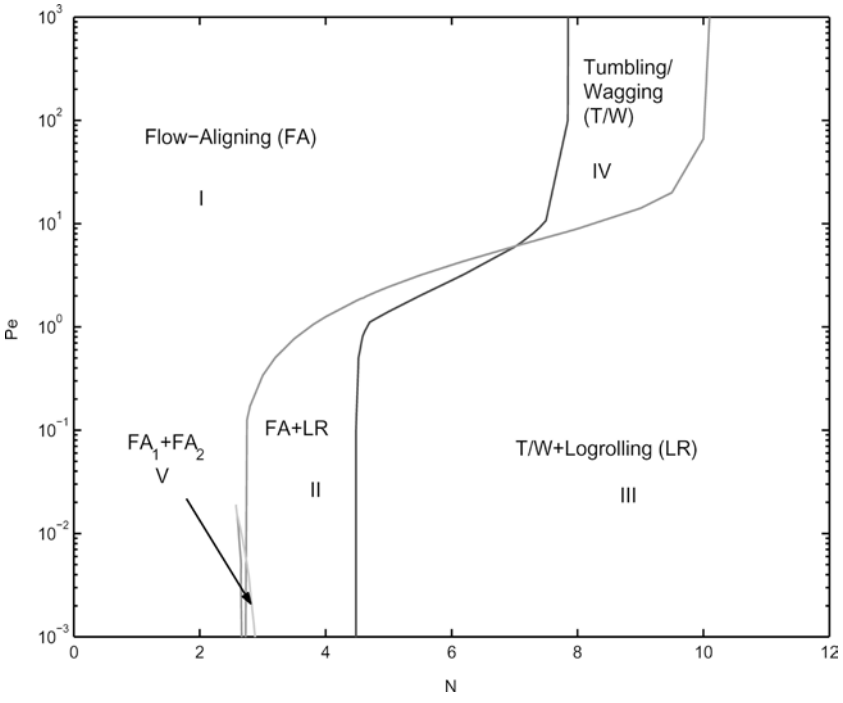

Fig. 1 The flow-phase diagram of the Doi closure model with constant rotary diffusivity, for confined *in-plane orientation tensors* and molecule aspect ratio $r = 3$ or 1/3. The diagram depicts all stable monodomain states versus nematic concentration (N) and normalized shear rate (Pe). The bifurcation curves bound regions of fixed number and type of attracting states, corresponding to flow and concentration-induced phase transitions among confined in-plane attractors

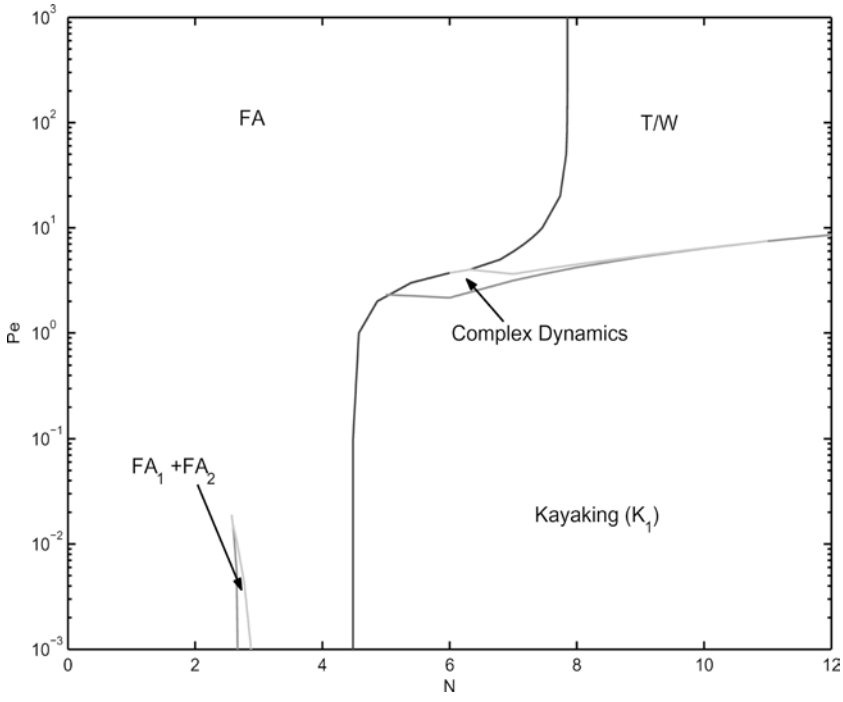

Fig. 2 The full tensor flow-phase diagram of the Doi mesoscopic closure model with constant rotary diffusivity, for aspect ratio $r=3$ or $1/3$, variable concentration (N), and normalized shear rate (Pe). The details of the "complex dynamics region" are discussed in [5]; see also [26]

Parametrization of the experimental initial data set

We study experimental systems beginning from rest. Therefore *the set of admissible data is given by the stable quiescent equilibria of the Doi model* (1)–(4), which consist of the isotropic phase $\mathbf{Q} \equiv 0$ for $N<3$, a bi-stable region for $8/3<N<3$, and the nematic region $N>3$, where the nematic phase is given by:

$$\begin{aligned} \mathbf{Q}(0) &= \mathbf{Q}_{\text{eq}} = s(N)\left(\vec{n}^t\vec{n} - \tfrac{\mathbf{I}}{3}\right), \\ \vec{n} &= (\cos\varphi_0 \sin\theta_0,\ \sin\varphi_0 \sin\theta_0,\ \cos\theta_0)^T, \\ &\quad \varphi_0 \in [0, 2\pi], \quad \theta_0 \in \left[0, \tfrac{\pi}{2}\right), \\ s(N) &= \frac{1+3\sqrt{1-8/(3N)}}{4} \in \left[\tfrac{1}{4}, 1\right], \text{ if } N > \tfrac{8}{3}. \end{aligned} \tag{6}$$

The bifurcations at $N=8/3$ and $N=3$ persist for $Pe>0$, and have been explained in detail by several authors [5, 7, 19, 20]. The third bifurcation curve in Fig. 1 and 2 which emanates from $Pe=0$ at $N\approx 4.5$ is more subtle, in that it is created by the flow perturbation. As detailed in [5, 7], this bifurcation corresponds to a steady-unsteady transition. Tumbling (**T**) emerges as the shear response for confined in-plane tensors (Fig. 1) called the **FA-T** transition; as seen from Fig. 2, however, out-of-plane kayaking $\mathbf{K}_1$ states also arise simultaneously with **T** states, and the **T** states are unstable to director tipping until much higher shear rates. To characterize the steady-unsteady transition curve of both phase diagrams, one considers the weak flow limit, from which a Leslie tumbling parameter λ_{Leslie} is derived, and the unsteady transition occurs when $\lambda_{\text{Leslie}} = \pm 1$. For the Doi closure one finds $\lambda^{\text{Doi}}_{\text{Leslie}} = \frac{a(2+s)}{3s}$. For $a = \pm 0.8$, and the equilibrium order parameter value $s = s(N) = \frac{1+3\sqrt{1-8/(3N)}}{4}$, one finds $N\approx 4.5$, as the numerical diagrams of Figs. 1 and 2 confirm.

Note that all nematic equilibria are orientationally degenerate, parametrized by $\vec{n} \in S^2$, with $\vec{n}$and $-\vec{n}$ identified. The degree of nematic ordering, $s(N)$, is uniquely prescribed by the nematic concentration N. As explained in [3, 21], for example, various techniques are utilized to control plate anchoring of $\vec{n}$, which then sets the monodomain equilibrium value for $\mathbf{Q}(0)$, at least near the plates. In typical samples there are many monodomains, corresponding to a distribution of $\vec{n}(0)$, for which a statistical study is relevant.

We also investigate the dynamics for special experimental major director data (θ_0, φ_0) from [22], to compare the behavior of their data set and predictions of the Leslie-Ericksen continuum model with our mesoscopic model statistics. Note that, in our choice of spherical coordinates, $\theta_0=0$ corresponds to vorticity-alignment and $\theta_0=\pi/2$ corresponds to in-plane alignment with in-plane angle φ_0. Only when $\theta_0=\pi/2$ is the range of φ_0 restricted from $[0,2\pi)$ to $[0,\pi)$.

Stress tensor

For monitoring the first and second normal stress differences and shear stress, we record the homogeneous stress tensor (apart from an isotropic pressure) [5]:

$$\begin{aligned}\tau = &(2\eta + 3vkT\zeta_3(a))\mathbf{D} \\ &+ 3avkT\left[\mathbf{Q} - N\left(\mathbf{Q} + \frac{I}{3}\right)\mathbf{Q} + N\mathbf{Q} : \langle \mathbf{mmmm}\rangle\right] \\ &+ 3vkT[\zeta_1(a)(\mathbf{DM} + \mathbf{MD}) + \zeta_2(a)\mathbf{D} : \langle \mathbf{mmmm}\rangle], \quad (7)\end{aligned}$$

where η is the solvent viscosity, $\zeta_{1,2,3}$ are three shape-dependent friction coefficients given in Appendix A; and v is the number density of LCP molecules per unit volume. The quantities $3v\mathrm{kT}\zeta_i$, $i=1,2,3$ are Doi analogs of Leslie viscosities. We remark that although the dynamics and stability properties of $\mathbf{Q}$ are trivially related by a rotation of the axes for rods ($a>0$) versus platelets ($a<0$), the stresses are dependent on the sign of a and the differences in friction coefficients. The impact of this effect on each type of monodomain attractor is reported in the figures.

Local and global measures of attractor "strength"

Local measure of strength for steady attractors

The traditional measure of stability for a **steady** solution is its linearized eigenvalues, which give all local decay rates for initial data that are sufficiently nearby the attractor. For this section, we employ the vector form, (1), of the dynamical system, and by slight abuse of notation, continue to use F and G for the corresponding vector fields.

Let $\bar{Q}$ be a steady solution from Fig. 1, either **FA** or **LR**. If we expand Q in a neighborhood of $\bar{Q}$, $Q = \bar{Q} + \tilde{Q}$, insert the expansion into (4), and retain terms linear in the perturbation $\tilde{Q}$, then

$$\begin{aligned}&\dot{\tilde{Q}} = \mathbf{L}\tilde{Q}, \\ &\mathbf{L} = \mathbf{L}(\bar{Q}; N, a, Pe) = DF(\bar{Q}; N, a) + PeDG(\bar{Q}, \nabla\mathbf{v}; a),\end{aligned} \quad (8)$$

where DF and DG are the first variations of F and G, evaluated at the equilibrium $\bar{Q}$.

For any steady state $\bar{Q}$, the linearized operator $\mathbf{L}$ is constant, and all linearized solutions $\tilde{Q}$ are constructed from the eigenvalues and eigenvectors of $\mathbf{L}$. We let $\left\{\tilde{Q}^{(1)}, ..., \tilde{Q}^{(5)}\right\}$ denote a basis of eigenvectors of $\mathbf{L}$, and let $\{\lambda_1,...,\lambda_5\}$ denote the corresponding eigenvalues, ordered by

$$Re(\lambda_5) \leqslant Re(\lambda_4) \leqslant Re(\lambda_3) \leqslant Re(\lambda_2) \leqslant Re(\lambda_1). \quad (9)$$

The steady state $\bar{Q}$ will be stable if $Re(\lambda_i)\leqslant 0$ for all i, and asymptotically stable if $Re(\lambda_i)<0$ for all i. Except possibly at the bifurcation curves of Figs. 1 and 2, all steady attractors have $Re(\lambda_1)<0$, and λ_1 is simple.

Consider any data $Q(0)$ in a small neighborhood of $\bar{Q}$ of size δ,

$$\left\|Q(0) - \bar{Q}\right\| = \left\|\tilde{Q}(0)\right\| = \delta, \ 0<\delta \ll 1. \quad (10)$$

Then the slowest decaying mode is either 1-dimensional (if $\lambda_1<0$) or 2-dimensional $\left(\text{if } \lambda_1 = \lambda_2^*\right)$. In either case the dominant term in the linearized solution $\tilde{Q}(t)$ for $t\gg 1$ is proportional to $e^{Re(\lambda_1)t}\tilde{Q}^{(1)}$. This allows one to infer a *local linearized timescale*, $t_{\text{local}} = -\frac{1}{Re(\lambda_1)}$, on which the initial data Q_0 contracts from a δ-radius ball around $\bar{Q}$ to a δ/e–radius ball. This picture of linearized flow near an attractor leads us to define a *local expected time of convergence to a steady stable state* $\mathbf{A}$,

$$\langle t_{\text{local}}\rangle_{\mathbf{A}} = -\frac{1}{Re(\lambda_1)}. \quad (11)$$

The local strength of $\mathbf{A}$ is then measured by how rapidly data converge to the attractor, so that

$$\text{'}\textit{local strength of attractor}\ \mathbf{A}\text{'} \quad \propto \quad \langle t_{\text{local}}\rangle_{\mathbf{A}}^{-1} \quad \propto \quad |Re(\lambda_1)|. \quad (12)$$

For example, if $Re(\lambda_1) \backsim -10^{-3}$, then $\bar{Q}$ is a very weak attractor, requiring $\langle t_{\text{local}}\rangle_{\mathbf{A}} \backsim 10^3$ dimensionless time units for nearby initial data to decay by a factor of e^{-1}. Recall we have normalized time by the average molecular relaxation time, which is on the order of 10^{-1}–10^2 seconds for typical nematic polymers.

Local measure of strength for periodic attractors

We now consider the linearized stability of periodic solutions, which we denote $\bar{Q}(t)$, with

$$\bar{Q}(t+T) = \bar{Q}(t), \quad T = \text{period}. \quad (13)$$

If we expand Q in a neighborhood of $\bar{Q}(t)$, $Q(t) = \bar{Q}(t) + \tilde{Q}(t)$, then the linearized equation for $\tilde{Q}(t)$has periodic coefficients given by $\bar{Q}$:

$$\dot{\tilde{Q}}(t) = \mathbf{L}(\bar{Q}(t); N, a, Pe)\tilde{Q}. \quad (14)$$

We summarize the basic elements of linear systems of the form (14), so-called Floquet theory. If $\tilde{Q}(t) = \left[\tilde{Q}^{(1)}, ..., \tilde{Q}^{(5)}\right]$is a fundamental matrix solution of (14), then $\tilde{Q}(t+T)$ is also a fundamental matrix solution since $\mathbf{L}(\bar{Q}(t))$ is periodic with period T. Therefore, there is a nonsingular matrix $C = \tilde{Q}(T)\tilde{Q}^{-1}(0)$such that

$$\tilde{Q}(t+T) = \tilde{Q}(t)C, \quad \tilde{Q}(t+nT) = \tilde{Q}(t)C^n. \quad (15)$$

The matrix C, called the transfer matrix, therefore characterizes the asymptotic behavior of all solutions of

(14); the eigenvalues ρ of C are the characteristic multipliers of (14) and any λ such that $\rho = e^{\lambda T}$ is a characteristic exponent of (14). The system (14) will be stable if all multipliers satisfy $|\rho_i| \leqslant 1$ (in other words the characteristic exponents satisfy $Re(\lambda_i) \leq 0$). In our system, we always have a simple multiplier 1 corresponding to an arbitrary phase shift of the periodic solution, *so we use the second largest multiplier ρ_2 to measure the slowest decay timescale*, which gives the estimate $\langle t_{local} \rangle_{\mathbf{A}} \sim 0(-T/\log(|f_2|)) = 0\left(\frac{-1}{Re(\lambda_2)}\right)$.

These local diagnostics do not apply to the experimental initial data set (6), which is generally far away from the steady or periodic attractors. The linearized diagnostics are however, predictors of expected-time to converge to attractors, and are accessible from the numerical dynamical systems software AUTO [23].

"Global" measure of strength of a steady attractor

From arbitrary initial data, the relevant questions are:

- Which attractor in parameter regions with multiple stable states does the data converge to?
- How long does it take to reach a prescribed neighborhood of that attractor?

For nonlinear systems, except in rare exactly solvable systems, these questions can only be answered by statistics of numerical solutions for arbitrary initial data. We now develop these statistics.

At selected locations (N,Pe) inside the regions of Fig.1 (the in-plane subspace $Q^{\text{i-p}}$), we monitor the eigenvalues $\lambda_j(t_n)$ of the local Jacobian, $\mathbf{L}(Q(t_n))$, which we then average over the attracting set for each steady attractor to construct $\langle Re(\lambda_j)(t_n) \rangle$, $j = 1, 2, 3$. We restrict to attractors away from the phase transition curves, since these bifurcations are often infinite-period, which will distort the statistics.

Statistics for low concentration, $N = 3.5$

To illustrate these ideas, we begin with the vertical slice, $N = 3.5$, of Fig. 1, whose attractors versus Pe are given in Table 1.

Table 1 Stable solutions of the Doi model versus Peclet number, for a fixed nematic concentration $N = 3.5$, and for a 1:3 discotic or 3:1 rod-like nematic polymer aspect ratios

Attractors	In-plane confined dynamics		Full tensor result
	FA + LR	**FA**	**FA**
Range of Pe	(0,0.77)	(0.77,10)	(0,10)

Let $\bar{Q}^{\mathbf{A}}$ denote the steady attractor, where $\mathbf{A} = \mathbf{FA}$ or **LR** for the in-plane subspace, whereas $\mathbf{A} \equiv \mathbf{FA}$ for the full tensor space. Note this information from Figs. 1 and 2 already conveys that the **LR** states of this model are all unstable to out-of-plane (director tipping) perturbations [5]. Indeed, **LR** stability is very sensitive to the closure rule [7]. Appealing to the Doi kinetic theory to resolve this issue, one finds a significant parameter regime of stable logrolling states for large N, and low Pe, see [8, 9], including bi-stable **T** and **W** states. Therefore, Figures. 1 and 2 show that the $Q^{\text{i-p}}$ model is more faithful to kinetic theory than the full tensor model in regard to preservation of **LR** attractors! We will return to this topic later, in the "In-plane bi-stable statistics" section.

We numerically solve both ODE systems ($Q^{\text{i-p}}$ and full Q) and monitor two measures of "distance between the orbit at time t and the attractor",

$$D_1 = \left\| \frac{Q(t) - Q^{\mathbf{A}}}{Q^{\mathbf{A}}} \right\|, \quad D_2 = \left\| \frac{Re(\lambda_1(t_n)) - Re(\lambda_1)}{Re(\lambda_1)} \right\|. \quad (16)$$

The first distance function $D_1(t)$ keeps track of the closeness of the tensors along the orbit $Q(t)$ to the respective attractor $Q^{\mathbf{A}}$, while the second distance function $D_2(t)$ monitors closeness of the maximum eigenvalues (slowest decay rate) of the linearized vector field along the orbit and at the steady state. We compute a family of orbits through the initial data set (6), by taking 100 choices for $\varphi(0) \in [0,\pi)$ for the $Q^{\text{i-p}}$ system, and 500 random choices, $(\varphi(0), \theta(0)) \in [0, 2\pi) \times \left[0, \frac{\pi}{2}\right]$ for the full tensor system. In regions with multiple attractors, we first compute which subsets of each data set ($\varphi(0) \in S^1$ or $(\varphi(0),\theta(0)) \in S^2$) converge to each attractor, and then sample from these attracting sets. We stop each orbit at $t_{\text{stop}}(\varphi(0))$ or $t_{\text{stop}}(\varphi(0),\theta(0))$, respectively, when $D_1(t)$ or $D_2(t)$ lies within a prescribed neighborhood.

Figure 3 compares the confined in-plane attractors and properties with the full tensor results. From Fig. 2 and Table 1, we fix $N = 3.5$ and $r = 1/3$ ($a = -0.8$) to compare with the in-plane results. The only full tensor attractor is **FA**, so the **LR** states are unstable to out-of-plane (director tipping) instabilities. For this reason, we don't give statistics of the **LR** state. *The key issue now is whether the slowest decaying mode to the* **FA** *state is in-plane, or out-of-plane*.

Conclusions from Fig. 3:

- Figure 3a: At $Pe < 4.8$, the slowest decaying modes are out-of-plane, whereas for $Pe > 4.8$ the out-of-plane linearized components decay on the same timescale (or even faster for higher Pe).
- Figure 3b: A similar qualitative behavior as Fig. 3a emerges for the global statistic, $\langle t \rangle_{\mathbf{FA}}$, though less significant differences are seen at low Pe. Taken together, these statistics imply that the transient dynamics dominates Fig. 3b at low Pe. Approxi-

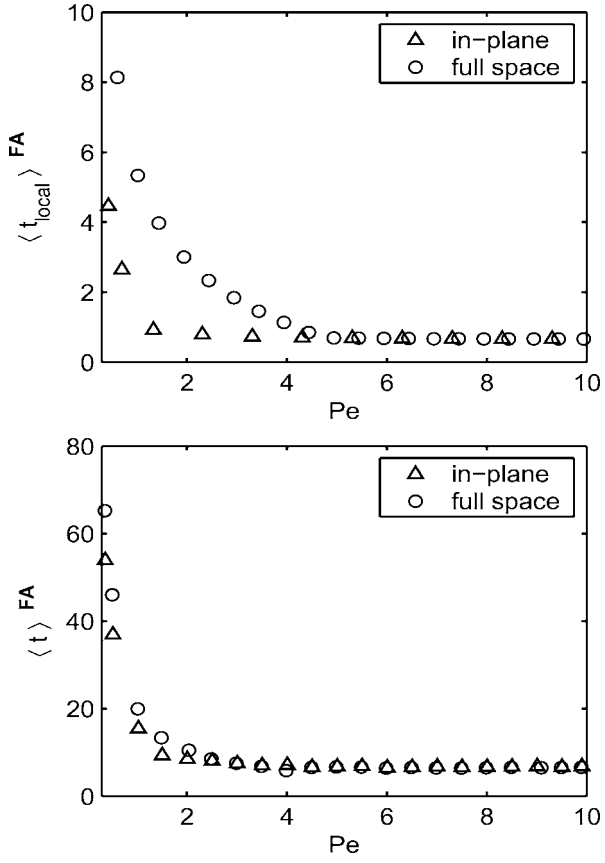

Fig. 3 In-plane statistics (top) versus that of the full tensor space (bottom) for the expected time to converge to flow-aligned steady states **FA**, with nematic concentration $N = 3.5$, distance function $D_2 < 10^{-3}$

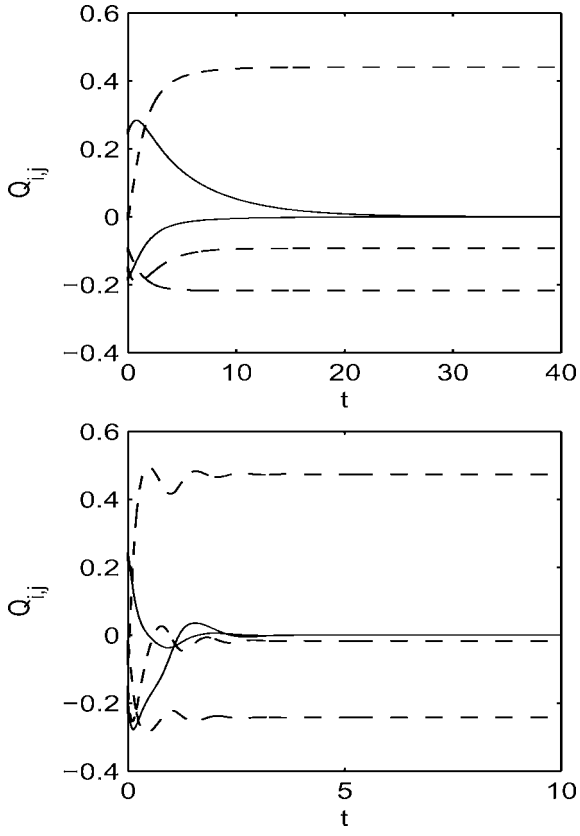

Fig. 4 Sample orbits to **FA** attractors for $Pe = 1$ (top) and $Pe = 10$ (bottom) in region I of Fig. 2, for $N = 3.5$. The dashed curves are the in-plane orientation tensor components, whereas the solid curves are the out-of-plane components Q_{xz}, Q_{yz}

mately 80% of the global statistic $\langle t \rangle_{\mathbf{A}}$ is spent getting to a neighborhood of the attractor. These transient properties are insensitive to the rods versus discotic aspect ratio $r = 3$ versus $r = 1/3$.

To illustrate the statistics of Fig. 3, we give details of selected sample orbits. For $Pe = 1$, from Fig. 4a (top), the out-of-plane components (solid lines) clearly converge to equilibrium values slower than the in-plane components (dashed lines). For $Pe = 10$, Fig. 4b (bottom) shows that the out-of-plane components converge at approximately the same rate as in-plane components.

Figures 5a,b indicate the rheological properties during the transient approach to the **FA** attractors depicted in Fig. 4. Recall that the first and second normal stress differences are $N_1 = \tau_{xx} - \tau_{yy}$, $N_2 = \tau_{yy} - \tau_{zz}$, and the apparent shear viscosity is $\eta = \tau_{xy}/Pe$. The transient rheology is surprisingly different at low and high shear rates: the high shear rate, strong attractor with short convergence time has stress oscillations in N_1 and η that do not show up in the low shear rate case. Furthermore, the shear stress (apparent viscosity) drops by approximately 40%, while the first normal stress differences increase by similar amounts, as Pe increases from 1 to 10. For a discotic aspect ratio $r = 1/3$, the steady state values and transient features of N_1 and η are similar for typical **FA** parameter regimes, while N_2 experiences a factor of four reduction in magnitude. In general, independent of the attracting state, $\langle N_1 \rangle$ and $\langle \eta \rangle$ are insensitive to rod versus platelet aspect ratio, whereas $\langle N_2 \rangle$ can be either larger or smaller in magnitude, as shown in later figures.

We now make comparisons of the Doi model with recent experiments and Leslie-Ericksen model predictions of [3] for **FA** nematic liquids. Figure 6 depicts the normalized Leslie alignment angle $\Phi = \frac{\phi - \phi_0}{\phi_L - \phi_0}$ as in [3]. To compare with their experimental data, we choose $N = 3.5$, $Pe = 1$ for rod-like nematic polymers with $a = 0.8$, which yields φ_L close to the equilibrium Leslie angle $\varphi_L = 8.5°$ of the Leslie-Ericksen model. As the out-of-plane tilt angle θ_0 ranges from $\theta = 9°$ (near the vorticity axis) to $\theta = 81°$ (near the shearing plane), Fig. 6a shows the transient major director goes from a strong overshoot to monotone convergence to the equilibrium φ_L. The out-of-plane polar angle θ, however, increases monotonically to 90° for all θ_0, Fig. 6b. These data show

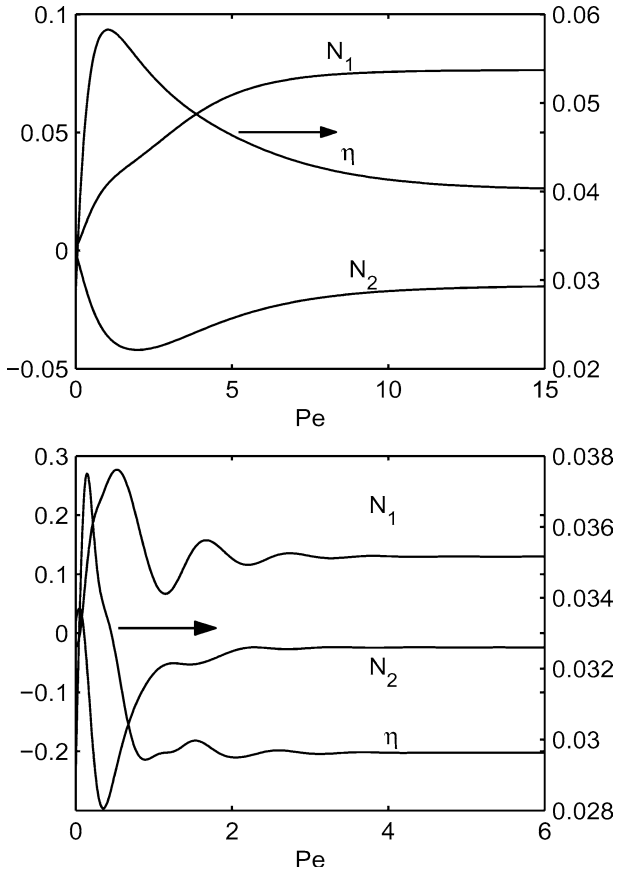

Fig. 5 First and second normal stress differences N_1,N_2 (left axis scale), and apparent viscosity η (right axis scale) versus time, for transient approach to the **FA** attractor of Table 1, with nematic concentration $N=3.5$, and rod-like aspect ratio $r=3$ ($a=0.8$), $Pe=1$ (top), $Pe=10$ (bottom)

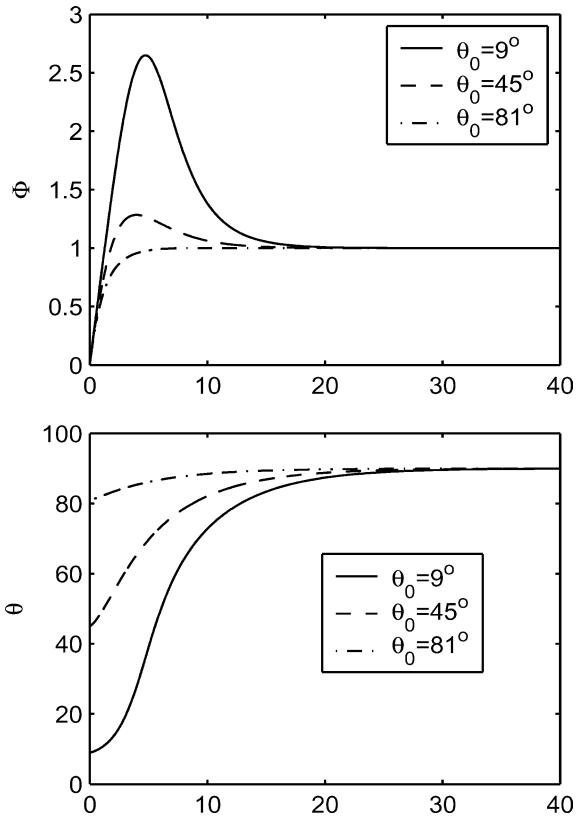

Fig. 6 Mesoscopic predictions for the start-up of shear flow of the relative Leslie alignment angle Φ with $\phi_0=3.6°$, $\phi_L=7.91°$, and initial out-of-plane tilt angles θ_0 with $\theta_0=9°$, 45°, 81°, respectively. $Pe=1$, $N=3.5$, $a=0.8$

that the mesoscopic tensor model reproduces Leslie-Ericksen behavior of the director only when the initial director is close to the shearing plane, even at low shear rates ($Pe=1$). The director overshoot behavior does not occur in the Leslie-Ericksen model [3]. The stress signature of the director overshoot of Fig. 6a is seen from Fig. 5a, which is a sample orbit corresponding to $\theta_0=45°$. We further note that the director and stress overshoot behavior is amplified at high shear rate, as seen at $Pe=10$ in Fig. 5b where $\theta_0=45°$ as well. As expected, the disparity between the mesoscopic tensor model and the Leslie-Ericksen model is quite significant at high shear rates.

Statistics for high concentration, $N=6$

We next increase the concentration to $N=6$ in Figs. 1 and 2, which accesses complex out-of-plane dynamics. For this subsection, we will focus on the **FA** states to distinguish high concentration from the low concentration **FA** states analyzed above.

Consider the **FA** states in Table 2. Figure 7 gives the expected time for convergence, which is very similar to the low concentration statistics of Fig. 3. When $3.117<Pe<5.1$, out-of-plane modes dominate the

Table 2 Stable solutions of the Doi tensor model versus Peclet number, for a fixed nematic concentration $N=6$, and for 1:3 discotic or 3:1 rod-like nematic polymer aspect ratios

Attractors	In-plane confined dynamics (see Fig. 1)			Full-tensor result (see Fig. 2)						
	LR + T/W	**FA + LR**	**FA**	$\mathbf{K_1}$	$\mathbf{K_1 + W}$	$\mathbf{K_2^{+,-} + K_1}$	$\mathbf{K_1 + CH}$	**CH**	$\mathbf{K_2^{+,-}}$	**FA**
Range of Pe	(0,2.819)	(2.819,3.979)	(3.979,10)	(0,2.162)	(2.162,2.405)	(2.405,2.536)	(2.536,2.923)	(2.923,3.245)	(3.245,3.717)	(3.717,10)

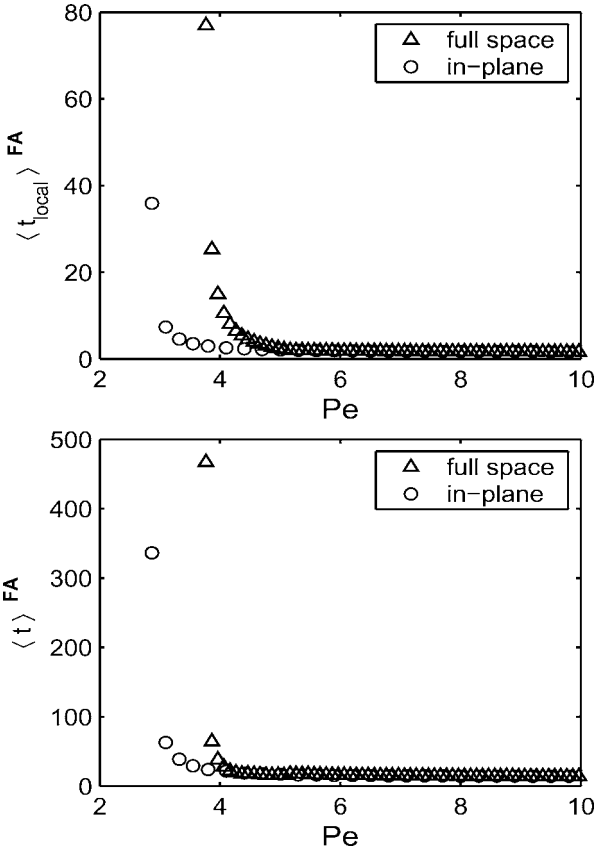

Fig. 7 In-plane statistics (top) versus that of the full tensor space (bottom) for the expected time to converge to steady flow-aligned states **FA**, fixed nematic concentration $N=6$, and distance function $D_2 < 10^{-3}$

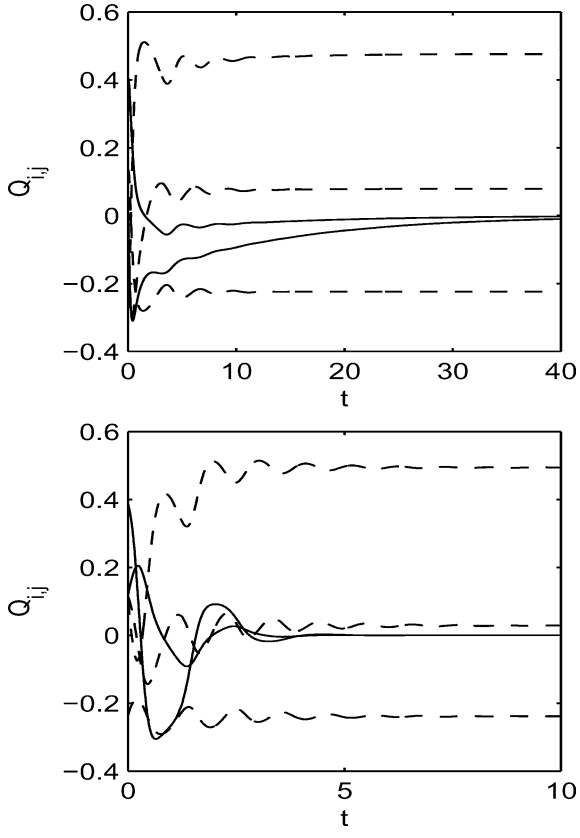

Fig. 8 Sample paths for **FA** attractors in the high concentration ($N=6$), strong shear ($Pe=4$, top; $Pe=10$, bottom) regime. The dashed curves are the in-plane orientation tensor components, whereas the solid curves are the out-of-plane components Q_{xz}, Q_{yz}

expected time, whereas for $Pe > 5.1$, the out-of-plane modes do not slow the convergence of purely in-plane dynamics.

Figure 8 illustrates the statistical averages of Fig. 7 with sample orbits. From Fig. 8a, the out-of-plane components (solid lines) converge to 0 slower than in-plane components (dashed lines) when $Pe=4$, but at $Pe=10$ all **Q** components converge on the same time-scale. At this high concentration, there is a high threshold shear rate to access the **FA** regime (see Fig. 2). At these high shear rates, all orbits converging to **FA** states have stress oscillations, independent of in-plane or out-of-plane behavior. This suggests that the stress oscillations are shear rate dependent and not associated with in-plane or out-of-plane degrees of freedom.

"Global" measure of strength of a periodic attractor

Now we proceed to discuss expected-time statistics for convergence to periodic solutions for $N=6$, Table 2. The components of **Q** trace out closed trajectories, and a different measure of distance from the attractor is required. We use the classic distance (D_3) from a point $\vec{Q}$ of the form (1) to a bounded set of points $\left\{\vec{Q}(j)\right\}_{j=1}^{M}$ for 5-dimensional vectors

$$D_3 = min\left\{\sum_{i=1}^{5}\left|\vec{Q}_i - \vec{Q}_i(j)\right|\right\}. \tag{17}$$

First we compute the limit cycle numerically, and then represent the orbit in terms of a set of M points, $\left\{\vec{Q}(j)\right\}_{j=1}^{M}$, uniformly distributed in Q-component space as opposed to distributed in time along the periodic orbit. The distance $\left\|\vec{Q}(j+1) - \vec{Q}(j)\right\|$ between two neighboring points on the orbit is set at 10^{-3}, which has been chosen such that robust statistics are achieved.

Next, we compute a family of orbits for random data chosen from the initial data set (6), and keep track of the distance between the trajectories and the attractor. We stop each orbit at t_{stop} when the distance lies within a prescribed neighborhood (10^{-3}) of the numerically resolved exact solution. We then confirm in selected cases

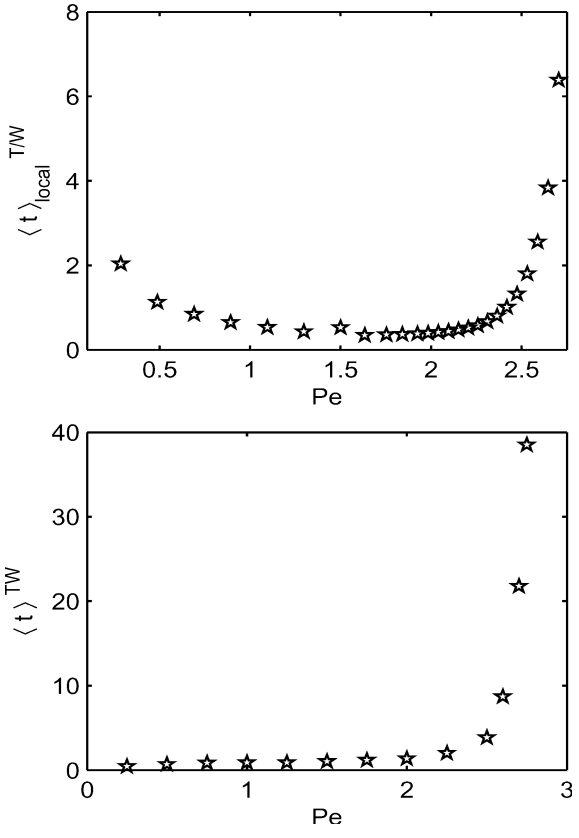

Fig. 9 In-plane statistics for the expected time to converge to **T**/**W** attractors of Table 2, for confined in-plane dynamics, with nematic concentration $N = 6$

that the trajectory stays in the small tube-like neighborhood of the periodic solution after t_{stop}.

To make things simpler, we consider the in-plane case first: Table 2 shows that **T**/**W** occurs for $Pe < 2.819$ for confined in-plane dynamics when $N = 6$. (Note these orbits are stable for $2.162 < Pe < 2.405$, but unstable in the $0 < Pe < 2.162$ full-tensor space to director tipping, but we suppress these degrees of freedom for Figs. 9 and 10.)

Figure 9a calculates $-T/(log(|\rho_2|))$, $T =$ period, which is the definition of $\langle t_{\text{local}} \rangle$. Figure 9b shows the global statistics, indicating that from a random initial condition, the trajectory rapidly converges to the tumbling or wagging attractor. Figure 10 shows the stress oscillations in the approach to and during a tumbling attractor, for a typical sample orbit. The first normal stress difference oscillates between positive and negative values. Within each period of the tumbling limit cycle, N_1 and η exhibit a long stress relaxation phase associated with the slow director and order parameter phase, interrupted by strong stress oscillations during the rapid resetting of the director. The model predicts three sign changes in N_1 per period. The order parameter s oscillates once per tumbling cycle with 13% variation in values, indicating significant molecular elasticity.

We now recognize that for $0 < Pe < 2.162$ the **T** and **W** attractors for $N = 6$ are unstable to out-of-plane (director tipping) instabilities. Nonetheless, if the initial director is aligned in-plane, there is a competition between strong in-plane convergence to **T** and **W** limit cycles, and relatively weak out-of-plane instability. We are therefore led to ask: if the **T** or **W** attractor is resonated, how many periods of the in-plane limit cycle are traversed before the orbit is expected to escape out-of-plane? This question is answered by the Floquet multipliers of Figs. 1 and 2, discussed in the previous section. For $N = 6$, $|a| = 0.8$, $Pe = 0.5$, the in-plane limit cycle is tumbling. We compute that the unstable Floquet multiplier is $\rho = 1.08$, the period $P_{\mathbf{T}}$ of the **T** orbit is $P_{\mathbf{T}} = 33$, from which we deduce the linearized timescale of instability, $t_{\text{inst}} = P/\log(\rho) \approx 13P_{\mathbf{T}}$. Therefore, it takes 13 director rotations or 430 relaxation units to escape the tumbling attractor! For $N = 6, |a| = 0.8$, $Pe = 2.02$, the in-plane attractor is wagging, with period $P_{\mathbf{W}} = 8.7$, the unstable multiplier is $\rho = 1.29$, which implies $t_{\text{inst}} \approx 4P_{\mathbf{W}}$ which means it takes four wagging cycles (35 relaxation time units) to escape out-of-plane. These properties suggest an experiment of limited duration would probably observe **T** or **W** transient behavior, although longer experiments will escape into out-of-plane response.

Next, we explore the expected convergence times for out-of-plane limit cycles. The above results, showing long times just to build up the out-of-plane components Q_{xz}, Q_{yz}, foreshadow long convergence times to the out-of-plane attractors.

For Fig. 2 and Table 2, the full tensor model for $N = 6$ has a complex shear response versus Pe. There are two types of kayaking attractors, the standard $\mathbf{K}_1$ whose major director rotates around the vorticity axis, and mirror-symmetric states $\mathbf{K}_2^{+,-}$ which occur in bi-stable pairs whose major director rotates between the vorticity axis and shearing plane [5, 6, 24, 25], Fig. 2, Table 2.

When $0 < Pe < 2.162$, the unique attractor is $\mathbf{K}_1$. Near $Pe = 0$ (Fig. 11), the extremely long convergence time reflects the infinite-period bifurcation from the orientationally degenerate nematic equilibrium to the $\mathbf{K}_1$ limit cycle [5, 7]. The period of $\mathbf{K}_1$ versus Pe is decreasing, and the expected time $\langle t \rangle_{\mathbf{K}_1}$ likewise decreases versus Pe (Fig. 11). At $Pe = 1$, $P_{\mathbf{K}_1} = 33.43$, and the expected convergence time is $\langle t \rangle_{\mathbf{K}_1} \approx 641$ relaxation time units. For $Pe \in (1.25, 2.1)$, $\langle t \rangle_{\mathbf{K}_1}$ ranges between 450–150 relaxation time units. As Pe approaches 2.923, the $\mathbf{K}_1$ attractors disappear through a turning point bifurcation [7]. We conclude attractors in weak shear are rarely (if ever) observed in the laboratory; rather, the transient behavior from the initial data is relevant. The statistical results support private communications by G. Berry, W. Burghardt, and P. Moldenaers, Pittsburgh 2003 Society of Rheology Meeting, who report they have never knowingly observed kayaking monodomains in their laboratories!

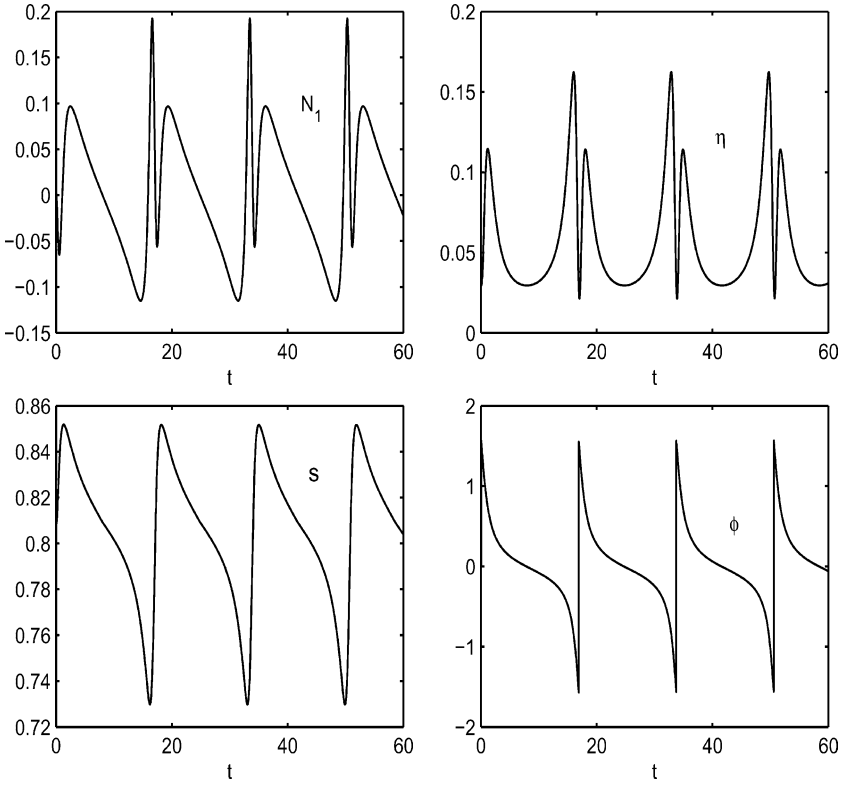

Fig. 10 First normal stress difference N_1 (top left), apparent viscosity η (top right) versus time, the corresponding time series of the order parameter (bottom left), and time series of the in-plane major director angle ϕ (bottom right), for a randomly chosen orbit converging to a **T** attractor of Table 2, with Peclet number $Pe=1$, nematic concentration $N=6$, and rodlike aspect ratio $r=3$ ($a=0.8$). The averages over one period are $\langle N_1\rangle\approx 1.7\times10^{-2}$, $\langle N_2\rangle\approx 6\times10^{-4}$(not shown), $\langle\eta\rangle\approx 7\times10^{-2}$, with large deviations by factors of 10 for N_1 and 2 for η. For a discotic aspect ratio $r=1/3$ ($a=-0.8$), $\langle N_1\rangle$ and $\langle\eta\rangle$ are quantitatively similar, whereas $\langle N_2\rangle$ is about a factor of 2 larger

For $2.162 < Pe < 2.405$, **W** orbits coexist with $\mathbf{K}_1$ attractors; the **W** attractors come and go through an instability transition. Figure 11a shows the slowest linearized convergence rates of $\mathbf{K}_1$ and **W** stable limit cycles, whereas Fig. 12 compares their periods. Note that $P_{\mathbf{W}} \approx \frac{1}{2}P_{\mathbf{K}_1}$ in this bi-stable region, so their "motion" is comparable. In the center of the stable **W** regime, $\langle t\rangle_{\mathbf{W}}^{\text{local}} \ll \langle t\rangle_{\mathbf{K}_1}^{\text{local}}$. Because the **W** attractor occurs over such a short Pe range, this "stiff" behavior is predicted where a **W** limit cycle is weakly then strongly then weakly attractive as Pe slowly rises. Note from Fig. 2 that the small shear rate window of **T**/**W** limit cycles for $N=6$ expands rapidly at higher N, while the complex dynamics region disappears.

Figure 13 shows the transient stress signature of a typical **W** limit cycle. The difference from the **T** attractor, Fig. 10, is that the stress spikes and is not as strong, N_1 only changes sign once per period, and the time-average of N_1 is negative. The apparent viscosity η changes sign once per period, dipping slightly below zero. The order parameter fluctuations are almost 100% during the wagging cycle, indicating dominant molecular elasticity. The order parameter and director dynamics are in phase, and do not reflect the secondary spikes in N_1 and η.

Figure 14 repeats Fig. 13 for the co-stable kayaking attractor. The signature of N_1 is remarkably similar for tumbling and kayaking; however, the apparent viscosity eventually loses the secondary oscillation or "double dip" per period once the limit cycle is reached. The order parameter oscillates in phase with the major director, though with smaller amplitude variations than the **W** attractor. The in-plane angle of the major director continues to rotate, while the out-of-plane angle oscillates over a finite range typical of the kayaking image of [17].

These sample orbits also illustrate the relatively large expected time for convergence to $\mathbf{K}_1$ versus **W** orbits: $\langle t\rangle_{\mathbf{K}_1} \approx 10\langle t\rangle_{\mathbf{W}}$, or about 100 relaxation time units. The period average of N_1 also has opposite sign: $\langle N_1\rangle_{\mathbf{W}}<0$, whereas $\langle N_1\rangle_{\mathbf{K}_1}>0$. We return to this bi-stable parameter region in the next section.

Domains of attractions in bi-stable and tri-stable regions

Figures 1 and 2 and Tables 1 and 2 indicate that sheared nematic polymers have significant (shear rate, concentration) regimes with multiple attracting states. Furthermore, since typical experimental samples consist of many monodomains, the measured rheology will be a statistical average over the distribution of attractors. In this section, we compute this distribution for selected parameter regimes with bi-stable and tri-stable monodomain modes.

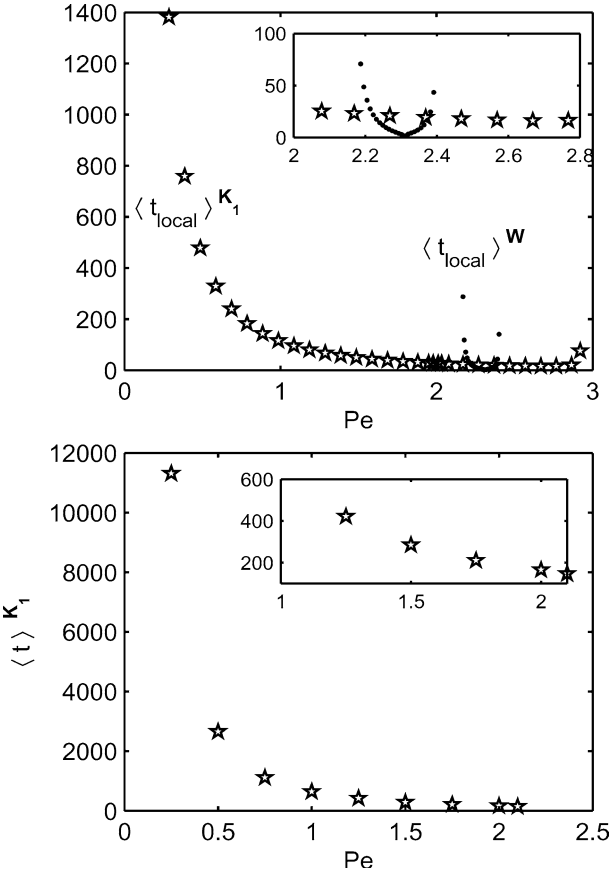

Fig. 11 Full tensor model statistics for the expected time to converge to the $\mathbf{K}_1$ attractor of Table 2, with $N=6$

In-plane bi-stable statistics

The first example is the bi-stable **LR**+**T** or **LR**+**W** regime of Fig. 1 and Tables 1 and 2, which is consistent with the kinetic phase diagram of [7]. By contrast, the full tensor diagram (Fig. 2) has spurious, closure-induced, out-of-plane **LR** instabilities. Therefore, the in-plane model is actually a more faithful approximation of kinetic theory for this bi-stable regime. Kinetic simulations were recently used [26] in the **LR**+**W** bi-stable regime to compare with experimental data for a distribution of **LR** and **W** attractors. They posited a (90%**W**, 10%**LR**) distribution, presumably from statistics. Here we compute the statistical distribution as follows. Because the model is confined in-plane, the nematic equilibrium initial data (6) is restricted to in-plane, with the major director in the plane or along the vorticity axis.

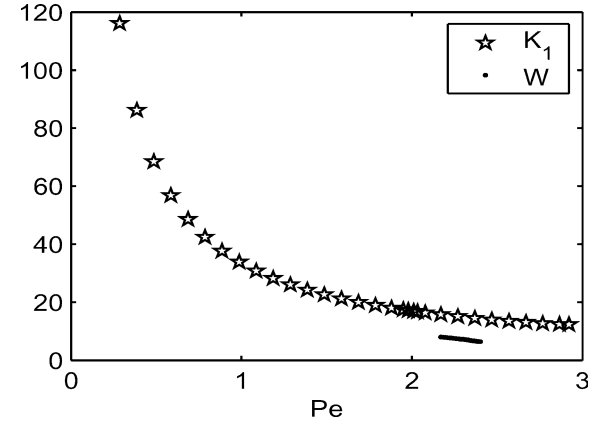

Fig. 12 Comparison of the limit cycle periods for **W** and $\mathbf{K}_1$ attractors

The dynamics of the in-plane model for this initial data is trivial: all in-plane data converge to the **T** or **W** attractor. Therefore, we completely randomize the initial data set to any $Q^{\text{i-p}}$ of the form:

$$Q = s\left(\vec{n}\vec{n} - \frac{\mathbf{I}}{3}\right) + \beta\left(\vec{n}^{\perp}\vec{n}^{\perp} - \frac{\mathbf{I}}{3}\right) \tag{18}$$

where $s=d_1-d_2$, and $\beta=d_2-d_3$; d_i, $i=1,2,3$ are the eigenvalues of Q, with $\vec{n} = (cos\varphi_0, sin\varphi_0, 0)$. Then we choose 1000 random data, parametrized by (s,β,ϕ_0), and count the percentage of data that converge to each attractor. This calculation literally gives the relative measure of the domains of attraction of **LR** and **T**/**W** attractors over the entire 3-dimensional phase space, which we call the likelihood of resonating each attractor. The same method is used for the **FA**-**LR** bi-stable steady parameter regime of Table 1.

Case 1. For fixed concentration $N=4$, we vary *Pe* in the **FA** and **LR** bi-stable region. Table 3 shows the distribution of arbitrary initial data (18) that converges to each attractor. Note that as *Pe* decreases, the likelihood of **LR** states grows.

Case 2. To compare with kinetic results of [26], we choose $N=6.66$ in Fig. 1, which is characterized by the co-existence of a stable **T**/**W** limit cycle with a stable **LR** solution. Table 4 shows the distribution of attractors. In the bi-stable **W**-**LR** regime, the likelihood of **LR** varies between 15% and 32%, but then jumps to 41% likelihood when bi-stable with **T** limit cycles.

Out-of-plane bi-stable and tri-stable statistics

From Fig. 2 and Table 2, we have a bi-stable $\mathbf{K}_1$ and **W** regime. Whenever the tilted kayaking limit cycle $\mathbf{K}_2$ is stable, it always has its bi-stable twin, on the other side of the shearing plane. We also have a tri-stable region of $\mathbf{K}_1$ and $\mathbf{K}_2^{+,-}$. We now measure the statistical likelihood of converging to each attractor from nematic equilibrium data.

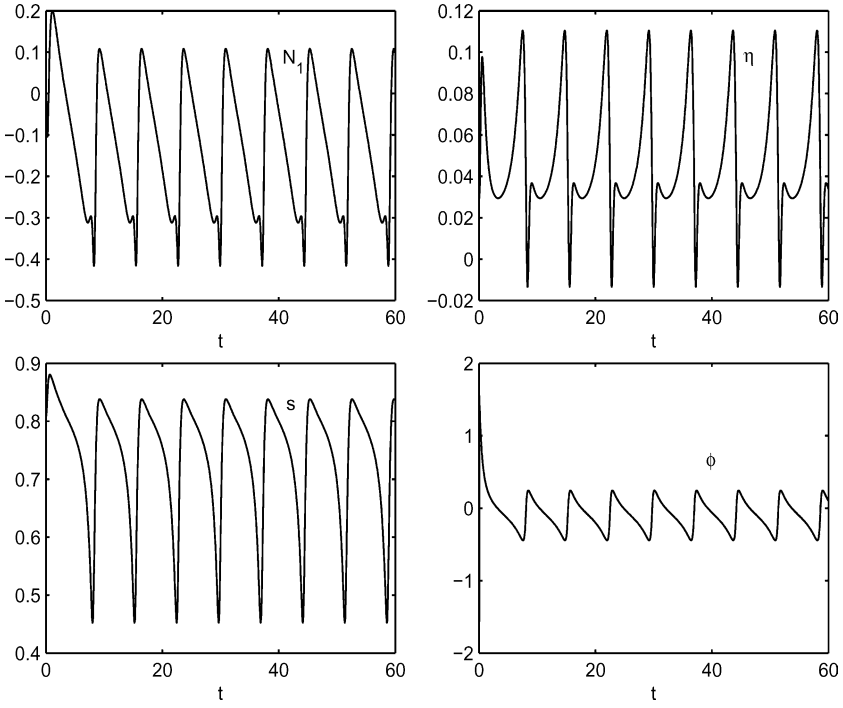

Fig. 13 First normal stress difference N_1 (top left), apparent viscosity η (top right) versus time, for a randomly chosen orbit that converges to the **W** attractor of Table 2, with Peclet number $Pe = 2.3$, nematic concentration $N = 6$, rodlike aspect ratio $r = 3$ ($a = 0.8$). $\langle N_1 \rangle \approx -1.1 \times 10^{-1}$, $\langle N_2 \rangle \approx 3.5 \times 10^{-2}$ (not shown), $\langle \eta \rangle \approx 4 \times 10^{-2}$ over the period of **W**, with strong fluctuations of factors of 3 for N_1 and 3 for η. The corresponding order parameter and in-plane director dynamics are shown bottom left and right. For a discotic aspect ratio $r = 1/3$ ($a = -0.8$) with all other parameters held constant, $\langle N_1 \rangle$ and $\langle \eta \rangle$ are nearly identical, while $\langle N_2 \rangle$ increases by a factor of about 2

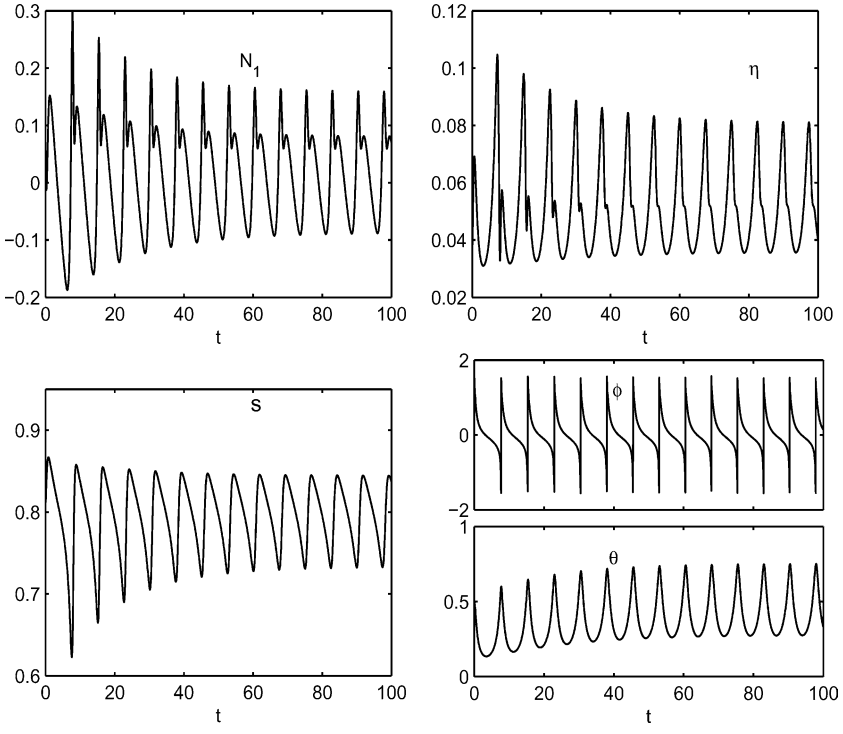

Fig. 14 First normal stress difference N_1 (top left), apparent viscosity η (top right) versus time, for a randomly chosen orbit that converges to the $\mathbf{K}_1$ attractor of Table 2, with Peclet number $Pe = 2.3$, nematic concentration $N = 6$, rodlike aspect ratio $r = 3$ ($a = 0.8$). $\langle N_1 \rangle \approx 4 \times 10^{-2}$, $\langle N_2 \rangle \approx -3 \times 10^{-2}$ (not shown), $\langle \eta \rangle \approx 5 \times 10^{-2}$ over the period of $\mathbf{K}_1$, with strong fluctuations of factors of 5 for N_1 and 2 forη. For discotic aspect ratio $r = 1/3$ ($a = -0.8$), $\langle N_1 \rangle$ and $\langle \eta \rangle$ are nearly the same, while $\langle N_2 \rangle$ decreases by a factor of 10

Case 1. When $Pe = 2.3$ and $N = 6$, the $\mathbf{K}_1$ and **W** bistable regime, Fig. 15 shows the statistical likelihood of convergence to $\mathbf{K}_1$ and **W** as the initial nematic director at rest is sampled across the sphere.

– If the initial directors $\vec{n}$ have polar angles $\theta_0 \geq 85.5°$, then all the data converge to the in-plane **W** attractor. Therefore, initial director orientations that are sufficiently close to the shearing plane are attracted to the **W** attractor. This has important consequences since plate preparations in Couette cells can strongly prejudice the director orientation of the rest state.

Table 3 Statistical distribution of attractors in the **FA** and **LR** bi-stable regime for $N=4$ and three different Pe values

Pe	1	0.5	0.1
%**LR**	27	39	50
%**FA**	73	61	50

Table 4 Statistical distribution of attractors in the **T**/**W** and **LR** bi-stable regime, for $N=6.66$ and five different Pe values

Pe	5	3	2.66	2.3	1
%**LR**	15	27	30	32	41
%**T**	0	0	0	0	59
%**W**	85	73	70	68	0

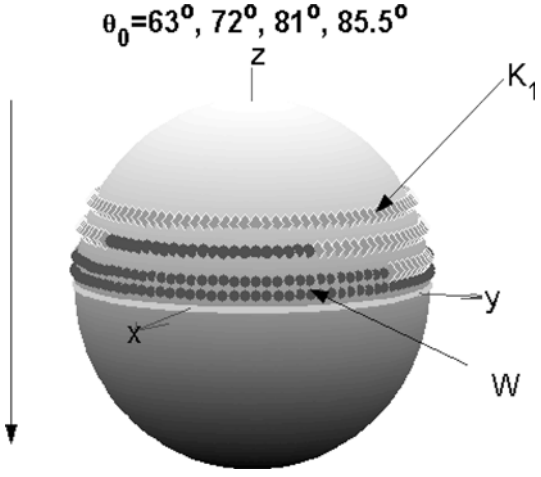

Fig. 15 Statistics of the likelihood of convergence to attractors from the nematic rest state at a fixed concentration $N=6$, for the $\mathbf{K}_1$ and **W** bi-stable region with $Pe=2.3$. The lighter points represent initial director configurations that will converge to $\mathbf{K}_1$, whereas the black points converge to **W**

- For initial directors $\vec{n}$ which have polar angles $\theta_0<63°$ (tilted sufficiently far from the shearing plane), all converge to the out-of-plane $\mathbf{K}_1$ attractor. Again, this has important experimental implications.
- Between these two "latitudes", there is no clear boundary for each attracting set. When θ_0 ranges between 81° and 68.4°, we find initial data with different in-plane tilt angles ϕ_0 converge to different attractors, shown in Table 5.
- As Pe varies over the range (2.162,2.405), which is the region of coexistence of $\mathbf{K}_1$ and **W** for $N=6$, the likelihood of convergence to $\mathbf{K}_1$ versus **W** varies, as shown in Table 6.

Combining these results with those from the previous section, we find that while the expected time to converge

Table 5 Likelihood statistics for $N=6$, $Pe=2.3$, in the **W** and **LR** bi-stable regime, with different initial polar angles. The degree of out-of-plane tilt is seen to control the likelihood of **W** vs **LR** attractors

θ_0(degrees)	81	76	72	68.4
%$\mathbf{K}_1$	20	36	56	80
%**W**	80	64	44	20

Table 6 Statistical distribution of bi-stable attractors for $N=6$, with different Pe values in the **W** and $\mathbf{K}_1$ bi-stable regime

Pe	2.2	2.3	2.4
%$\mathbf{K}_1$	92.5	83.2	77
%**W**	7.5	16.8	23

to **W** attractors $\langle t\rangle_{\mathbf{W}}$ is much shorter than $\langle t\rangle_{\mathbf{K}_1}$, the attracting set of $\mathbf{K}_1$ is larger than that of **W** if the initial data consists of randomly oriented nematic rest states. However, initial pre-alignment of monodomains can strongly bias the distribution in favor of in-plane **W** attractors!

Figure 16 shows the time series of averaged N_1, N_2 and η over 1000 random sample orbits, and the average values of N_1, N_2 and η are approximately the weighted average (83% of $\mathbf{K}_1$, 17% of **W**) of $\mathbf{K}_1$ and **W**. $\langle N_1\rangle\approx -7\times10^{-3}$ is almost negligible [26].

Case 2. Figure 17 shows the statistics when we increase Pe to 2.5, the $\mathbf{K}_1$, $\mathbf{K}_2^{+,-}$tri-stable regime.

- If the initial directors $\vec{n}$ have polar angles $\theta_0\geq 81°$, all data converge to the $\mathbf{K}_2$ attractor. Initial directors that are sufficiently close to the shearing plane are attracted to one of the $\mathbf{K}_2$ orbits!
- Initial directors with polar angles $\theta_0<49.5°$ (tilted toward the vorticity axis) all converge to the $\mathbf{K}_1$ limit cycle.
- Table 7 and Fig. 17 show that the likelihood of $\mathbf{K}_1$ versus $\mathbf{K}_2^{+,-}$varies dramatically when the initial polar angle θ_0 ranges between 81° and 49.5°.

Remark: Through explicit solution of the model equations, we compare properties of $\mathbf{K}_1$ versus $\mathbf{K}_2^{+,-}$ attractors. We find the out-of-plane components Q_{xz} and Q_{yz} of $\mathbf{K}_2$ attractors are always less than that of $\mathbf{K}_1$ limit cycles. Therefore, it is reasonable to believe that if the initial director $\vec{n}$is near the shearing plane, it is more likely to converge to either of the $\mathbf{K}_2$ states, while if the initial director is near the vorticity axis, then the data are attracted to the $\mathbf{K}_1$ state.

Table 8 shows that as Pe increases in the interval (2.405,2.546), the likelihood of $\mathbf{K}_1$ attractors decreases to about 70%. Overall however, the domain of attraction of $\mathbf{K}_1$ is greater than the $\mathbf{K}_2^{+,-}$pair.

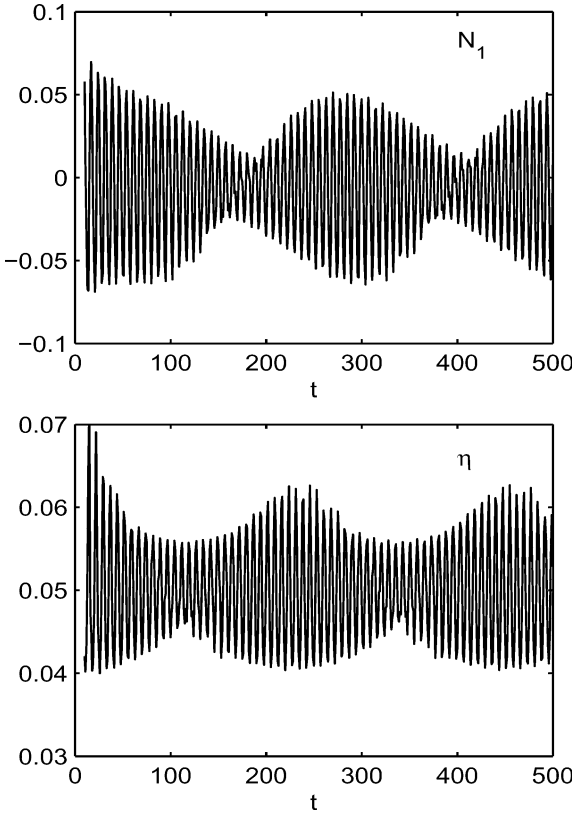

Fig. 16 First normal stress difference N_1 (top), apparent viscosity η (bottom) versus time, averaged over 1000 sample orbits in the bi-stable region of Table 2, with Peclet number $Pe = 2.3$, nematic concentration $N = 6$, rodlike aspect ratio $r = 3$ ($a = 0.8$). $\langle N_1 \rangle \approx -7\times10^{-3}$, $\langle N_2 \rangle \approx 1.5\times10^{-2}$ (not shown), $\langle \eta \rangle \approx 5\times10^{-2}$, with strong fluctuations of factors of 6 for N_1 and 1.3 for η. The results for platelets ($a = -0.8$) are nearly identical for $\langle N_1 \rangle$ and $\langle \eta \rangle$, whereas $\langle N_2 \rangle$ is nearly zero, but negative

Table 7 Attractor likelihood distribution for $N = 6$, $Pe = 2.5$, which is in the $\mathbf{K_1}$ and $\mathbf{K}_2^{+,-}$ tri-stable regime, with different initial polar angles

θ_0 (degrees)	76.5	72	63	68.4
$\%\mathbf{K}_1$	16	26	48	92
$\%\mathbf{K}_2^{+,-}$	84	74	52	8

Table 8 Likelihood statistics for $N = 6$ and different Pe in the $\mathbf{K_1}$ and $\mathbf{K}_2^{+,-}$ tri-stable regime

Pe	2.45	2.5	2.53
$\%\mathbf{K}_1$	74.1	71.4	70
$\%\mathbf{K}_2^{+,-}$	25.9	29.6	30

Case 3. We increase Pe to 3.5, where the $\mathbf{K}_1$ orbits have disappeared, Table 2, with only bi-stable $\mathbf{K}_2^{+,-}$. Figure 18 shows that $\mathbf{K}_2^{+}$ and $\mathbf{K}_2^{-}$ have the same strength at each latitude; the data will converge to each attractor with probability 1/2. They have the same strength and size. The expected time for a random initial condition to converge to $\mathbf{K}_2^{+,-}$ is about 200 relaxation time units.

Conclusions

We have provided a summary of experimentally relevant, statistical properties of nematic polymer monodomains in simple shear. These data indicate the expected time for steady states (flow-aligning and log-

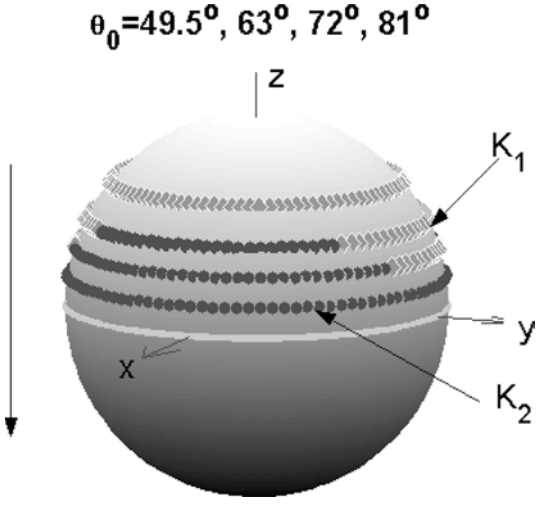

Fig. 17 Statistics in the tri-stable ($\mathbf{K}_1$, $\mathbf{K}_2^{+,-}$) region with $Pe = 2.5$. The lighter gray points on the sphere are the initial director orientations that converge to $\mathbf{K}_1$; the black points converge to $\mathbf{K}_2^{+,-}$

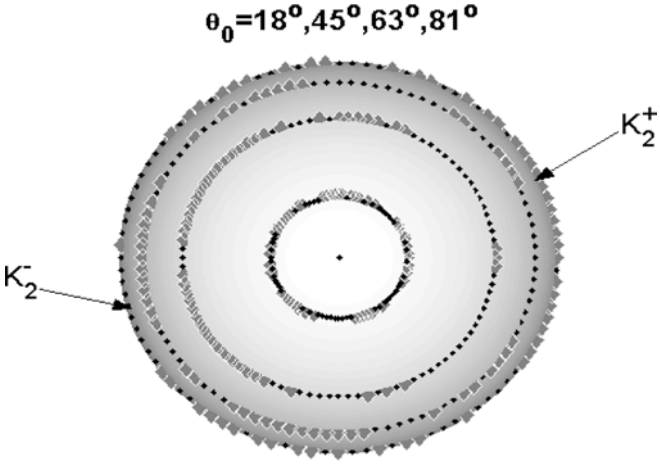

Fig. 18 Statistics in the $\mathbf{K}_2^{+,-}$ bi-stable region with $Pe = 3.5$. The light gray points are the initial director orientations that converge to $\mathbf{K}_2^{+}$, the black points converge to $\mathbf{K}_2^{-}$. Note that this view is looking down from the vorticity axis at the center

rolling attractors) and limit cycles (kayaking, tumbling, wagging, and chaotic attractors) to appear when shear experiments begin from rest. We have also determined the likelihood of convergence to individual attracting states when there are two or three stable monodomains. This statistical property allows one to predict rheological features of an experiment over a weighted average of the two or three attractor types. Finally, the transient rheology of each attractor is also shown, which conveys stress and orientational signatures from onset of shear, through the transients (which range from short to very long timescales), and finally of the attracting state. One clear outcome of this statistical study is that pre-alignment of the director orientation is a significant factor in the transient rheology of sheared nematic polymers. Furthermore, in-plane states such as flow-aligning, tumbling and wagging are relatively strong attractors, whereas out-of-plane kayaking limit cycles require extremely long timescales to be resonated. For parameter regimes where kayaking is the dominant attractor, the relevant model predictions for experimental comparison are the transient dynamics from startup of shear.

A. Viscosity coefficients of the Doi theory

$$
\begin{aligned}
&\eta_s = \eta + 3/2 vkT\zeta_3,\\
&\zeta_3 = \frac{\zeta^{(0)}}{I_1},\ \zeta_1 = \zeta^{(0)}\left(\frac{1}{I_3}-\frac{1}{I_1}\right),\ \zeta_2 = \zeta^{(0)}\left[\frac{J_1}{I_1 J_3}+\frac{1}{I_1}-\frac{2}{I_3}\right],\\
&I_1 = 2r\int_0^\infty \frac{dx}{\sqrt{(r^2+x)}(1+x)^3},\ I_3 = r\left(r^2+1\right)\int_0^\infty \frac{dx}{\sqrt{(r^2+x)^3}(1+x)^2},\\
&J_1 = r\int_0^\infty \frac{xdx}{\sqrt{(r^2+x)}(1+x)^3},\ J_3 = r\int_0^\infty \frac{xdx}{\sqrt{(r^2+x)^3}(1+x)^2}
\end{aligned}
\qquad \text{(A1)}
$$

Acknowledgements This work was sponsored by the Air Force Office of Scientific Research, Air Force Materials Command, USAF, under grant no. F49620–02–1-0086, and the National Science Foundation through grants DMI-0115445, DMS-0204243 and DMS-0308019. The work was supported in part by the NASA University Research, Engineering and Technology Institute on Bio Inspired Materials (BIMat), under award no. NCC-1–02037.

References

1. Larson RG, Ottinger H (1991) Macromolecules 24:6270–6282
2. Larson RG (1999) The structure and rheology of complex fluids. Oxford University Press, Oxford, UK
3. Van Horn BL, Boudreau DM, Winter HH (2003) Rheol Acta 42(6):585–589
4. Rey AD, Tsuji T (1998) Macromol Theor Simul 7:623–639
5. Forest MG, Wang Q (2003) Rheol Acta 42:20–46
6. Faraoni V, Grosso M, Crescitelli S, Maffettone PL (1999) J Rheol 43:829–843
7. Forest MG, Zhou R, Wang Q (2003) J Rheol 47(1):105–127
8. Forest MG, Wang Q, Zhou R (2003) Rheol Acta 43(1):17–37
9. Forest MG, Wang Q, Zhou R (2003) Rheol Acta (submitted)
10. Grosso M, Keunings R, Crescitelli S, Maffettone PL (2001) Phys Rev Lett 86(14):3184–3187
11. Beris AN, Edwards BJ (1994) Thermodynamics of flowing systems with internal microstructure. Oxford University Press, Oxford, UK
12. Rienacker GR, Hess S (1999) Physica A 267:294–321
13. Forest MG, Wang Q, Zhou R (2002) Phys Rev E 66(3):031712
14. Fuller GG (1995) Optical rheometry of complex fluids. Oxford University Press, Oxford, UK
15. Marrucci G, Maffettone PL (1989) Macromolecules 22:4076–4082
16. Maffettone PL, Grosso M, Friedenberg MC, Fuller GG (1996) Macromolecules 29:8473–8478
17. Maruyama T, Fuller GG, Grosso M, Maffettone PL (1998) J Non-Newtonian Fluid Mech 76:233–247
18. Yao L, Zheng X, Forest MG, Wang Q, Zhou R (2004) A model for defect dynamics in sheared nematic polymers. University of North Carolina Program in Applied Mathematics Preprint, Chapel Hill, NC
19. Doi M (1981) J Polym Sci Pol Phys 19:229–243
20. Larson RG (1990) Macromolecules 23:3983–3992
21. Tan ZJ, Berry GC (2003) J Rheol 47:73–104
22. Van Horn BL, Winter HH (2000) Rheol Acta 39:294–300
23. Doedel EJ, Champneys AR, Fairgrieve TF, Kuznetsov YA, Sandstede B, Wang X (1997) AUTO97: Continuation and bifurcation software for ordinary differential equations. Concordia University, Montreal, Canada
24. Rienacker GR, Kroger M, Hess S (2002) Phys Rev E 66:040702
25. Hess S (2003) Z Naturforsch A 58:377–391
26. Grosso M, Crescitelli S, Somma E, Vermant J, Moldenaers P, Maffettone PL (2003) Phys Rev Lett 90:098304